Contribution in optimization of Zn Cold-sprayed coating dedicated to corrosion applications

E. Lapushkina, S. Yuan, N. Mary, J. Adrien, Kazuhiro Ogawa, Bernard Normand

Version of Record: https://www.sciencedirect.com/science/article/pii/S0257897220308628
Manuscript_052fad3a86a61df8dfe15c4c0b61d81e

Contribution in optimization of Zn Cold-sprayed coating dedicated to corrosion applications.

E. Lapushkina[1,2], S. Yuan[1], N. Mary[2], J. Adrien[1], K. Ogawa[2,3], and B. Normand[1*]

[1]Université de Lyon, INSA Lyon, CNRS, MATEIS UMR 5510, Villeurbanne, France
[2]Université de Lyon, CNRS, ELyTMaX UMI 3757, Tohoku University, Sendai, Japan
[3]Tohoku University, Fracture and Reliability Research Inst, Aoba-ku, Sendai, Japan

*Corresponding author
B. Normand
Campus LyonTech-La Doua
20 Avenue Albert Einstein 69621 Villeurbanne Cedex, France.
Tel. +33 (0)4 72 43 62 87,
bernard.normand@insa-lyon.fr

Abstract

Cold spray coatings elaboration requires optimization of numerous parameters in order to reach the best coatings' performances. A systematic approach can be avoided by using an experimental design. A Doehlert uniform shell design was applied in this work to Zn cold sprayed coating. Coating were produced on steel substrates to provide high corrosion resistant layers. N_2 temperature and gas pressures varied from 200°C to 320°C and from 2.0 MPa to 3.0 MPa, respectively. Performance maps were plotted for two descriptors: (i) the interfacial porosity volume (substrate coating interface defects), (ii) coating thickness (i.e., coating durability), and validated with the polarization resistance (i.e., corrosion resistance). Results reported three set of optimized temperature and gas pressure values according to the descriptor.

Two optimized protection modes can be obtained: a sacrificial mode from heterogeneities in the coating (290 °C and 3.0 MPa), and a barrier protection mode from homogeneous and dense coatings (320 °C and 2.5 MPa). Mechanism of corrosion have been investigated.

Keywords: Experimental design; Cold spray; Zn; Coating; Corrosion; Electrochemistry

1. Introduction

Zn is a versatile material that can be used in several applications, including structural and protection [1-6]. It can be manufactured as a bulk material or coating. For the latter, the primary function is to protect structural metals against corrosion. Zn-coated steel is obtained by several processes such as hot-dip galvanizing, electro-galvanizing, and painting with Zn-bearing paints [2, 7]. The interest of Zn for corrosion protection is dual. It has a very low corrosion potential in the galvanic series (-0.79 V compared to the standard hydrogen electrode). This position implies a sacrificial character (dissolution) when Zn is coupled with a material with a higher potential. For example, it is the case for a porous Zn coating on a noble substrate. On the other hand, due to its passive character, a homogeneous Zn coating is able to form protective oxidation products that impede further corrosion when coating is free of pores [8]. In most cases, Zn layers behave as sacrificial coatings [9].

Alternative solutions emanated from spray techniques such as thermal or cold spraying [10-14]. The main difference between these two techniques relates to the physical state of Zn powder in the propellant gas. During thermal spraying, the gas temperature is higher than the melting temperature (solidification process), whereas the temperature remains below the melting point during cold spraying (solid deposition process). Because it is a flexible technique, cold spraying has gained popularity since the last decade. Moreover, it provides an efficient solution for on-site local restoration of damaged areas [15, 16] by performing either thin or thick coatings [9, 17, 18].

Because the particle experience different thermo-mechanical histories in thermal and cold spraying, the adhesion and the manufacturing mechanisms of the so-prepared coatings are also different. With cold spraying, the accumulation of the material is assured by the impact-induced bonding under a high-impact velocity. Several mechanisms have been proposed in literature to explain this phenomenon, such as adiabatic shear instability, oxide

layer breakup, mechanical interlocking, etc. [19, 20, 21]. Hassani-Gangaraj et al. argued recently that, if adiabatic shear instability prevails, a hydrodynamic jetting mechanism may occur instead of adiabatic processes [22]. Whatever the mechanism, cold spray coatings exhibit a microstructure comparable to highly cold-worked bulk material where defects (porosities, oxide, impurities, etc.) located mainly on the particle boundaries [23].

Metallurgical defects in cold-spray coatings decrease the corrosion resistance. They promote a path for solution propagation to the substrate [23, 24]. Thus, the addition of ceramic particles was proposed to densify the coating by decreasing the density of the pores [23, 25].

To improve the coating's performance, several input parameters in the cold spray technique need to be optimized, for instance, the working gas, gas temperature, gas pressure, the feedstock powder morphology, gun traverse speed, and number of passes, and stand-off distance of the spraying. Because all parameters are interdependent, a strategy is required to determine the optimal deposition parameters. The role of each parameter on coating physicochemical properties, morphology (thickness, roughness), and density (porosity, homogeneity) regarding corrosion resistance mitigation have been developed in [26]. The uniform design method was developed in [27] for the optimization and to evaluate the weight of each parameter. In another work, Phani et al. observed from Tagushi's method that a higher gas temperature has a positive effect on decreasing the porosity of a Cu coating [28]. In contrast, the increase in the stand-off distance from 5 to 25 mm slightly decreases the density of the coating.

This study aimed to investigate the correlation between input parameters of cold spraying and coating anticorrosion performances. Zn was selected as the sacrificial element for a cathodic coupling with steel [29]. Authors found only a few studies on such systems prepared by cold spraying [11, 30-33]. A dense and homogeneous Zn coating provides barrier

protection for steel against aggressive environments. The formation of oxide or hydroxide layers on the coating surface and in pores, promoting healing phenomena [8, 9, 34-35].

An experimental design was applied in this study to lower the experiment number [36]. In this study, we focused on the effect of the propellant gas temperature and pressure on the coating's porosity and thickness. The trends obtained from the experimental design were compared with corrosion performances evaluated from electrochemical measurements. Adhesion and roughness of the coatings have been characterized by bending tests and profilometry, respectively.

2. Doehlert uniform shell design

In literature, several experimental design exist, such as Taguchi [37-39], Plackett-Burman [37, 40-41], Box-Behnken [38, 40, 42], factorial [43, 44], simplex [38, 43], star [37, 41], Fang and Wang statistical experiment method [28], and central composite designs [37, 40-41]. Due to the clarity of results, the ease of interpretation, the Doehlert uniform shell design [36, 38, 40] was selected among them. The name "uniform shell design" means uniform distribution of the points or selected parameters on a spherical shell surface (Figure 1). The Doehlert design experimental points are located on the surface of a hyper-sphere for $k > 3$ variables. Experimental points for two and three variables are enclosed into a sphere with a radius of 1 (Figure 1a). Figure 1b shows the projecting section of the sphere in two dimensions, providing a combination of the different variables at every experimental point. When η is the total number of experimental combinations and k is the number of variables, η can be described as follows:

$$\eta=k^2+k+1 \quad (1)$$

For two variables, seven experiments have to be selected, and their spatial distributions will form a hexagon with a central point (Figure 1). In this study, the variables

X1 and X2 corresponded to the temperature and pressure of the spraying gas (Table I), respectively.

3. Materials and experimental procedure

3.1. Feedstock materials

Carbon steel plates with a chemical composition of 0.08–0.13% C, 0.15–0.35% Si, and 0.30–0.60% Mn were used as the substrates. Samples with dimensions of 3 cm × 7 cm × 1 mm were sand-blasted using Al_2O_3 (P100) under optimized conditions established in a previous study [23]. This treatment mechanically removed the native oxide from the surface, thereby increasing the sample roughness to attain higher mechanical adhesion to Zn particles.

Commercial gas-atomized Zn powder was provided by Grillo (Germany) and had a purity of 99.9%. Figure 2a shows the particle morphology. Powder morphology was a mix between spherical and elongated particles. The particle size distribution was measured using laser diffractometry (Mastersizer 2000, Malvern Instruments Ltd., UK). The mean diameter was deduced to 37.3 µm (+20 –90 µm) (Figure 2b). The plate of bulk zinc with dimensions 70x25x2 mm^3 and purity 99,9 % was provided by Goodfellow.

3.2. Cold Spray parameters

Zn coatings were prepared with the cold spray system Impact Spray System ISS 5/8-N-2 PF (Impact Innovations, Germany). The spray gun was mounted on a robot with a stand-off distance of 30 mm, a traverse speed fixed at 200 mm/s, and a distance between gun passes of 1 mm. The nozzle-substrate angle was fixed at 90°. The converging-diverging de Laval nozzle made of SiC had a length of 160 mm and the expantion ratio was 5.6 . Pure N_2 was used as the gas carrier with a flux of 50 m^3/h. The coatings were elaborated with one scan.

The gas temperature and pressure were the two variables to be adjusted according to the Doehlert uniform shell design. The boundary conditions were between 100 and 320 °C for

the gas temperature (melting point of Zn is 420 °C) and between 2 to 3 MPa for the gas pressure. A preliminary study was performed before selecting the spray parameters. As shown in Figure 3, when the temperature is lower than 230°C, the coating thickness remains low. Beyond this limit temperature, the coating thickness increase dramatically. -in Table I; seven corresponding coatings were obtained.

3.3. Metallographic and surface characterizations

The surface and cross-section of the Zn coating were observed using scanning electron microscopy (SEM Supra55, Zeiss, Germany) coupled with an 80 mm^2 Oxford energy-dispersive X-ray spectroscope (EDS) probe for analysis of the elemental chemical composition. The Zn coating surfaces were observed using a confocal optical microscope (Hirox HK7700, Japan). Careful cross-section preparation with the use of ethanol instead of water have been performed for all the samples. The roughness (due to high amplitude and a non-constant homogeneity called waviness) was distinguished by measuring the amplitude between the highest and lowest points on the surface of the coatings. Additionally, arithmetic roughness values R_a and R_z were calculated using a contact profilometer (Mitutoyo, Japan). The length of measurement and scanning rate were 2 cm and 0.5 m/s, respectively, and the cut-off filter λ_c 0.8/5 (mm)/L.

Phase identifications were based on the correlation of X-ray diffraction (XRD) peaks from the International Centre for Diffraction Data (ICDD) database. XRD diagrams were created using a Phillips PW 1830/40 diffractometer ($Cu_{K\alpha}$ at 20 kV and 10 mA). The volume percentages of porosity in coatings were evaluated via X-ray tomography using an EasyTom tomograph (RX Solutions, France). High-resolution images were acquired on small coated samples (2 mm× 2 mm× 30 mm) with a voxel size of 1 μm^3. This resolution was ensured by a LaB_6 emission tip for the X-ray source for which the resolution was not modified by

geometric blur. The A Hamamatsu X-Ray source was operated at a voltage of 100 kV with a 0.1 mm-thick copper filter.

Adhesion properties were defined from bending tests (Figure 4). Three-point bending tests were performed using a Zwick-Roell machine and TestXpert II software. A bending force was applied to the sample at a speed of 0.5 mm/min; the diameter of the cylinder tip was 8 mm. The length between the loading tip and supporting points was set as 30 mm (*L*) symmetrically on both sides . The coating was placed on the opposite side of the load tip.

The corrosion behavior of Zn coating was derived from electrochemical measurements. A standard 3-electrode electrochemical cell and Gamry Ref600 (USA) potentiostat were used. The working electrode was the coating with an apparent surface of 0.28 cm^2, and the reference and counter electrodes were a mercury saturated electrode (E_{MSE} = 0.658 V/NHE) and carbon rods of 6.7 cm^2, respectively. The open-circuit potential (OCP) was recorded for 6 h, and linear sweep voltammetry (LSV) was performed from –0.1 to 2 V according to the OCP with a scan rate of 1 mV/s. The electrolyte was an aerated and unstirred 0.1-M Na_2SO_4 solution at pH 6.5 and 20°C. OCP and LSV curves were also plotted on the Zn plates (99.9% purity, Goodfellow) to compare the electrochemical behavior of bulk materials with cold-sprayed Zn coatings. The corrosion current density (I_{corr}) was extracted using EC-Lab software from the Tafel plot extrapolation at the corrosion potential considering a charge transfer control and uniform corrosion.

4. Results

4.1. Coating roughness and surfaces

Different coatings were elaborated at the gas temperatures and pressures shown in Table II. 3D images of the surfaces were recorded using a confocal microscope. Because the waviness of all coatings were comparable, only the morphology of the coating performed at 320 °C and 2 MPa is depicted in Figure 5a. The surface consisted of valleys and hollows with

an amplitude of up to 91 µm. During the preliminary test, with a constant gas pressure of 2 MPa, we can observe the variation of the waviness amplitude as a function of the temperature from 100 to 320 °C. The maximum variation was observed at 260 °C (Table II).

The measurements of R_a and R_z using a contact profilometer indicated decreasing roughness as temperature increased (Figure 5b). This trend is attributed to a higher deformation of the particles on the surface caused by thermal softening. The upper layer of adhered particles exhibited a weak deformation compared with the dense inner layers (Figure 6).

4.2. Cross-section Microstructures

Figure 6 shows the cross-sections of the Zn coating performed at 260 °C and 2.5 MPa. The coating is dense, but with some interfacial defects that will be discussed in the next sub-section. The roughness of the substrate affected the coating adhesion. When the waviness of the substrate was not consistent with the particle size and deformation, weak interlocking occurs while gas was entrapped. However, coating delamination or cracks were not detected, which meaning an excellent adhesion between Zn and steel. After chemical etching, particle stacking was observed in Figure 7. A single pass of the spraying torch results seven layers of particles, approximately. No new phase or oxidation product in the coatings was detected by X-ray diffraction, as shown in Figure 8.

Table III shows the thicknesses of the coatings measured from the cross-section. A maximum thickness of 115 µm was obtained at 260 °C and 2.5 MPa, and a minimum value of 60 µm was obtained at 230 °C and 3 MPa.

4.3. Coating porosities

Because surface preparation can affect the quantifications of porosity, X-ray tomography tests were performed. Figure 9 shows only two typical tomography due to the

similarity among all samples. The highest heterogeneity was identified at the coating-substrate interface, highlighting the contribution of the roughness of the substrate on the interlocking process of Zn particles. The heterogeneity could be a result of internal stresses created by the effect related to the different natures of the powder and substrate materials. By image analysis of the volume, the percentage of the porosity volume was extracted for each condition. Regardless of the conditions, the amount of porosity within the coatings remains very low from 0.1 to 0.5%.

Besides, the coating/ substrate interface porosity depended on the spray conditions and surface preparation by sand-blasting. Keeping the same sand-blasting condition, the difference in the interface reflects the influence of the spray parameters primarily. Table IV shows low interfacial porosity percentages for all sample, among thema maximumvalue of 4% was obtained with a gas temperature and pressure of 290 °C and 3 MPa, respectively.

The interfacial porosity is generated by the recovery of Zn-particles on a rough substrate surface. If the particle velocity is low, there is a low particle deformation that can not mask the underlying roughness fully. However, an excessively strong particle impact can increase internal stresses at the interface or abrasive wear of the as-deposited coating layer [41]. However, a rebound effect of the particles occurs if the particle energy is too low to ensure adhesion [46].

4.4. Adhesion properties of coatings

The bending test was selected to evaluate the adhesion properties of defects placed mostly at the interface; the defects served as stress concentration and led to coating deadhesion. Figure 10a shows the plot of coating loading under straining is shown. All the curves indicated a constant elastic deformation with continuous loading from 0 to 350 N. Above 400 N, the elastic deformation became plastic one for all the samples. No damage to the coatings was observed during the test. The SEM of the cross-section of the coatings did

not reveal any cracks or delamination at the bent area; thus, the adhesion of coating was considered very high (Figure 10b).

4.5. Corrosion performance of Zn cold spray coatings

Figure 11a depicts the OCP evolution of the zinc coatings, composed of carbon steel and the bulk zinc sample. In an aerated and unstirred 0.1M Na_2SO_4 solution, all the potentials attained a steady state in the first seconds of immersion. As expected from the thermodynamic tables, Zn materials attained cathodic potential (–1.5 V/MSE) before carbon steel (–0.4 V/MSE), confirming its sacrificial role. At this stage, the effect of porosity in different samples at the coating/ substrate interface could not be detected. Thus, the waviness and particle deformation modifications with the spray condition were considered. However, the variation in potential among the seven samples was not significant to indicate any trends.

Figure 11b shows the linear sweep voltammograms recorded after OCP and the representative curves. The electrochemical behavior of the samples exhibited cathodic and anodic domains. The latter indicated the charge transfer that allowed the use of Tafel plot extrapolation to quantify I_{corr} at the corrosion potential (E_{corr}). At overpotentials (+0.3 V/E_c), limiting currents were detected at 10 mA/cm² that is characterized by the mass transport of dissolved species (Zn^{2+}). In the cathodic domain, the reduction of the media and the native oxide-hydroxide layers on Zn were expected. Zn oxide and hydroxide ratios slightly differed because of the local variation in pH due to the waviness of the surfaces. The current densities recorded for the bulk Zn and coating (1–10 mA/cm²) were higher than that of the steel (10 µA/cm²).

The corrosion current density and corrosion potential were calculated based on the Tafel plot approximation. Since the solution was aerated, the kinetics was partially controlled by the diffusion of dissolved oxygen. The corrosion resistance for each sample R_p was

estimated in a potential range of ±20 mV around E_{corr} for each sample. Table V lists the corrosion potential (E_{corr}), the polarization resistance (R_p), and the current of corrosion (I_{corr}).

Regarding the density of the coating, corrosion was primarily due to the waviness rather than porosity. In Table V, higher roughness indicates higher corrosion current density. High roughness induced the occluded cells, which initiated localized corrosion. The corrosive solution propagated into the coating through the pathway formed by the different heterogeneities. As the porosity level in the coating body was rather low, the corrosive media penetrated mainly through the interlamellar boundaries [23].

Figure 12 shows cross-sections of the coating after the electrochemical tests (7 h at OCP and LSV from OCP to 1.5 V). As the potentials of all the coatings indicated similar values, only the cross-section of one coating with spraying parameters of 290 ºC and 3 MPa after the LSV test was investigated.

The dissolution of the coating was observed from the top layer. The thickness decreased twice comparing with the initial state, which was approximately 60 µm as shown in Figure 12a. Some non-dissolved particles were still present, indicating that the weakest sites of the coatings were the boundaries between the deformed particles and the substrate-coating interface. Some parts of the coating dissolved, generating the defects at the coating/ substrate interface.

Some of the particles may have separated from the coating before their total dissolution. EDS analysis confirmed that the oxidation mostly occurred at the surface or at the coating/ substrate interface, as shown in Figure 12b. It should be mentioned that the defects were not generated by the preparation process (cut, polishing,…) since they can not be observed with no-corroded samples in Figure 6).

5. Discussions

Figure 13a shows the evolution of the interfacial porosity with the propellent gas temperature and pressure. The major part of the diagram reveals low porosity. The higher porosity corresponds to a high pressure and moderate temperature in the range of 260 °C< T < 300 °C. which promoted erosion of the substrate, as mentioned before, and lower accommodation of particles at the impact.

The limit temperature that ensures good adhesion of the particles, and its accumulation on the substrate was 230 °C. Under this temperature, the cold spray is not efficient, which was confirmed by the analysis of the thickness diagram showing lower thickness than other parts, see Figure 13b. Besides, thicker coatings were obtained at higher temperatures to promote the particle deformation combining with a moderate pressure that allows to limit erosion phenomenon. Thus, the temperature range is estimated from 230 to 320 °C, and the pressure ranges varies from 2.0 to 2.6 MPa to obtain thick coatings.

Corrosion performances were evaluated from electrochemical measurements to understand the role of previous trends. The analysis was based on polarisation resistance, and the results are shown in Figure 14. The higher values of polarization resistance were shown in the upper part of the diagram, where the maximum R_p was obtained at 3.0 MPa and 290 °C. It is interesting to notice that the maximum R_p was recorded with a relatively thin coating with high interfacial porosity. As mentioned in the previous part, a defective coating potentially promotes cathodic protection by forming a galvanic coupling with the substrate, which accelerates Zn dissolution. As reported by Souto et al., corrosion products induce self-healing and inhibitive protection [8].

A higher corrosion resistance was also obtained at a higher temperature (280 °C<T<320 °C) and medium pressure (2.5 MPa). This set of parameters promoted thicker and denser coatings. Thus, the corrosion performances were affected by the Zn coatings. No

sacrificial effect was observed, but corrosion resistance was governed by Zn corrosion behavior controlled by Zn hydroxide and oxide layers.

As Figures 13a and b indicate, because the porosity rate was lower and thickness higher for 260 °C and 2.5 MPa, the coating properties promoted a higher corrosion resistance. However, the polarisation resistance was not optimum. This result can be explained by remembering that roughness promotes corrosion initiation; thus, a higher roughness increases corrosion initiation. As Figure 5b shows, this was the scenario at 260 °C and 2.5 MPa, and explains the lower corrosion resistance of this set of parameters than 320°C and 2.5 MPa.

The best compromise was observed at 320 °C and 2.5 MPa. A high quality of Zn coating could be obtained that exhibited low porosity, larger thickness, and high corrosion resistance. This coating had the lowest interfacial porosity (0.8%) and a high coating thickness of 108 µm when the corrosion resistance was also high at 1347 Ω/cm^2.

6. Conclusions

- The Doehlert uniform shell design is a useful method to lower the number of experiments. This paper describes the effect of gas temperature and pressure on the coating microstructure and predicates further changes in the microstructure.
- Different sets of parameters enable two protection modes: the sacrificial mode for heterogeneities in the coating (290 °C and 3.0 MPa), and corrosion product protection for homogeneous and dense coatings (320 °C and 2.5 MPa).
- The mechanism of corrosion is described as conditioned by corrosion initiated by roughness and corrosion propagation through interlamellar microstructure controlled by an adiabatic shearing.
- A temperature of 320 ºC and pressure 2.5 MPa are the set of parameters that provide the highest corrosion performances of Zn cold spray coatings.

Acknowledgements

E. Lapushkina's PhD is supported by the Ministry of Education, Research and Innovation. This research was conducted in collaboration with ElyTMax UMI CNRS. Thanks to Pascal Reynaud from MATEIS (UMR CNRS 5510) for his contribution to the bending test.

7. References

[1] American Welding Society, Committee on Thermal Spraying, Corrosion Tests of Flame Sprayed Coated Steel, 19-Year Report, C2 ed. Miami (1974) 14-74 ISBNS: 9780871711113

[2] Metals HandBook, Properties and Selection: Nonferrous Alloys and Special-Purpose Materials, ASM nternational, 2 (1990). ISBN10 0871703785

[3] R. V. Dennis, L. T. Viyannalage, T. K. Rout, and S. Banerjee, Graphene nanocomposite coatings for protecting low alloy steels from corrosion, American Ceramic Society Bulletin, 92-5 (2013) 18-24. ISBN: 0002-7812

[4] S. Majumdar and P. Banerji, Hopping conduction in nitrogen doped ZnO in the temperature range 10–300 K, Journal of Applied Physics, 107 (2010) 6. doi: 10.1063/1.3353862

[5] S. Bonk, M. Wicinski, A. W. Hassel, and M. Stratmann, Electrochemical characterizations of precipitates formed on Zn in alkaline sulphate solution with increasing pH values, Electrochemistry Communications, 6-8 (2004) 800–804. doi: 10.1016/j.elecom.2004.05.012.

[6] A. P. Yadav, Electrochemical Impedance Response of Zn and Galvanized Steel Corroding under Marine Atmospheric Environments, Journal of Nepal Chemical Society, 23 (1970) 33–42. doi: 10.3126/jncs.v23i0.2094.

[7] R. Brindha, B. Karthigai Selvii, M Selvam, Corrosion Behavior of Zn/Graphene Composite in Aqueous Electrolyte System, J Nanosci Nanotechnol, 2 (2018) 303 ISSN: 2577-7920

[8] R.M. Souto, B. Normand, H. Takenouti, M. Keddam, Self-healing processes in coil-coated cladding studied by the scanning vibrating electrode, Electrochimica Acta, 55-15, 1 (2010) 4551-4557. doi:10.1016/j.electacta.2010.03.008

[9] N. M. Chavan, B. Kiran, A. Jyothirmayi, P. S. Phani, and G. Sundararajan, The Corrosion Behavior of Cold Sprayed Zn Coatings on Mild Steel Substrate, Journal of Thermal Spray Technology, 22-4, (2013) 463–470. doi: 10.1007/s11666-013-9893-z.

[10] G. Sundararajan, N. M. Chavan, G. Sivakumar, and P. Sudharshan Phani, Evaluation of Parameters for Assessment of Inter-Splat Bond Strength in Cold-Sprayed Coatings',

Journal of Thermal Spray Technology, 19-6 (2010) 1255–1266. doi: 10.1007/s11666-010-9527-7.

[11] C.-J. Li, W.-Y. Li, and Y.-Y. Wang, Formation of metastable phases in cold-sprayed soft metallic deposit, Surface and Coatings Technology, 198-1–3, (2005) 469–473. doi: 10.1016/j.surfcoat.2004.10.063.

[12] Y. Xiao, X. Jiang, Y. Xiao, and L. Ma, Research on Zn-Al15 thermal spray metal coating and its organic painting composite system protection performance, Procedia Engineering, 27 (2012) 1644–1653. doi: 10.1016/j.proeng.2011.12.632.

[13] H. Koivuluoto, P. Vuoristo (2014) Structure and corrosion properties of cold sprayed coatings: a review, Surface Engineering, 30:6, 404-413, doi: 10.1179/1743294413Y.0000000201

[14] A. Moridi, S. M. Hassani-Gangaraj, M. Guagliano, M. Dao (2014) Cold spray coating: review of material systems and future perspectives, Surface Engineering, 30:6, 369-395.,doi: 10.1179/1743294414Y.0000000270

[15] J. Fiebig, E. Bakan, T. Kalfhaus, G. Mauer, O. Guillon, R. Vaßen, Thermal Spray Processes for the Repair of Gas Turbine Components, Adv. Eng. Mater. 2020, 1901237, 1-11, doi : 10.1002/adem.201901237

[16] W. Li, K.Yang, S.Yin, X. Yang, Y. Xu, R. Lupoi, Solid-state additive manufacturing and repairing by cold spraying:A review, Journal of Materials Science & Technology 34 (2018) 440–457, doi: 10.1016/j.jmst.2017.09.015

[17] F. Wang, M. Zhao, Simulation of Particle Deposition Behavior in Cold-Sprayed Mg Anticorrosion Coating, Materials and Manufacturing Processes, 31 (2016) 11,1483-1489, DOI: 10.1080/10426914.2014.952042

[18] X.-T. Luo, Y.-J. Li, C.-X. Li, G.-J. Yang, C.-J. Li, Effect of spray conditions on deposition behavior and microstructure of cold sprayed Ni coatings sprayed with a porous electrolytic Ni powder, Surface & Coatings Technology 289 (2016) 85–93, doi: 10.1016/j.surfcoat.2016.01.058

[19] M. Grujicic, C. L. Zhao, W. S. DeRosset, and D. Helfritch, Adiabatic shear instability based mechanism for particles/substrate bonding in the cold-gas dynamic-spray process, Materials & Design, 25- 8 (2004) 681–688. doi: 10.1016/j.matdes.2004.03.008.

[20] H. Assadi, H. Kreye, F. Gärtner, and T. Klassen, Cold spraying – A materials perspective, Acta Materialia, 116 (2016) 382–407. doi: 10.1016/j.actamat.2016.06.034.

[21] J.G. Legoux, E. Irissou, C. Moreau, Effect of Substrate Temperature on the Formation Mechanism of Cold-Sprayed Aluminum, Zinc and Tin Coatings, Journal of Thermal Spray Technology, Volume 16, 5-6 (2007) 619-626. doi: 10.1007/s11666-007-9091-y.

[22] M. Hassani-Gangaraj, D. Veysset, V. K. Champagne, K. A. Nelson, and C. A. Schuh, Adiabatic shear instability is not necessary for adhesion in cold spray, Acta Materialia, 158 (2018) 430–439. doi : 10.1016/j.actamat.2018.07.065.

[23] Y. Wang, B. Normand, N. Mary, M. Yu, H. Liao, Effects of ceramic particle size on microstructure and the corrosion behavior of cold sprayed SiCp/Al 5056 composite coatings, *Surface & Coatings Technology* 315 (2017) 314–325. doi: 10.1016/j.surfcoat.2017.02.047

[24] A. Venugopal, R. D. Angal, and V. S. Raja, Effect of Grain-Boundary Corrosion on Impedance Characteristics of an Aluminum-Zn-Indium Alloy in 3.5% Sodium Chloride Solution, Corrosion, 52-2 (1996) 138–142. doi: 10.5006/1.3292104.

[25] K. Spencer, D. M. Fabijanic, and M.-X. Zhang, The use of Al–Al2O3 cold spray coatings to improve the surface properties of magnesium alloys, Surface and Coatings Technology, 204-3 (2009) 336–344. doi: 10.1016/j.surfcoat.2009.07.032.

[26] S. M. Hassani-Gangaraj, A. Moridi & M. Guagliano (2015) Critical review of corrosion protection by cold spray coatings, Surface Engineering, 31:11, 803-815, DOI:10.1179/1743294415Y.0000000018.

[27] J. F. Li, H. Liao, B. Normand, C. Cordier, G. Maurin, J. Foct, C. Coddet, Uniform design method for optimization of process parameters of plasma sprayed TiN coatings, Surface and Coatings Technology, 176-1 (2003) 1–13. doi: 10.1016/S0257-8972(03)00019-7.

[28] P. Sudharshan Phani, D. Srinivasa Rao, S. V. Joshi, and G. Sundararajan, Effect of Process Parameters and Heat Treatments on Properties of Cold Sprayed Copper Coatings, Journal of Thermal Spray Technology, 16-3 (2007) 425–434. doi: 10.1007/s11666-007-9048-1.

[29] A. Bai, K.-L. Yang, H.-L. Chen, Y. Hong, and S.-B. Chang, High current density on electroplating smooth alkaline Zn coating, MATEC Web Conf., 123 (2017) 00024. doi: 10.1051/matecconf/201712300024.

[30] H. Kim, B. N. Popov, and K. S. Chen, Comparison of corrosion-resistance and hydrogen permeation properties of Zn–Ni, Zn–Ni–Cd and Cd coatings on low-carbon steel, Corrosion Science, 45-7 (2003), 1505–1521. doi: 10.1016/S0010-938X(02)00228-7.

[31] J. G. Legoux, E. Irissou, and C. Moreau, Effect of Substrate Temperature on the Formation Mechanism of Cold-Sprayed Aluminum, Zn and Tin Coatings, Journal of Thermal Spray Technology, 16-5-6 (2007) 619–626. doi: 10.1007/s11666-007-9091-y.

[32] Z. B. Zhao, B. A. Gillispie, and J. R. Smith, Coating deposition by the kinetic spray process, Surface and Coatings Technology, 200-16–17 (2006) 4746–4754. doi: 10.1016/j.surfcoat.2005.04.033.

[33] W.-Y. Li, C.-J. Li, and G.-J. Yang, Effect of impact-induced melting on interface microstructure and bonding of cold-sprayed Zn coating, Applied Surface Science, vol. 257-5 (2010) 1516–1523. doi: 10.1016/j.apsusc.2010.08.089.

[34] A. R. Marder, The metallurgy of Zn-coated steel, Progress in Materials Science, 45-3 (2000) 191–27. doi: 10.1016/S0079-6425(98)00006-1.

[35] G. E. Dieter, Effects of Surface Treatments on Materials Performance, in Materials Selection and Design, Ed. ASM International, 20 (1997) 470–490. doi.10.31399/asm.hb.v20.a0002466

[36] P. Araujo and S. Janagap, Doehlert uniform shell designs and chromatography, Journal of Chromatography B, 910 (2012) 14–21. doi: 10.1016/j.jchromb.2012.05.019.

[37] O.Y. Rodionova, R.G. Brereton, Chemometrics: Data Analysis for the Laboratory and Chemical Plant, Journal of Analytical Chemistry, Chichester: Wiley, 60-10 (2005) 994-996, doi: 10.1007/s10809-005-0223-6

[38] O. Sailer, Thomas P. Ryan, Modern Experimental Design: Wiley, Statistical Papers, 49-3 (2008) 597–598. doi: 10.1007/s00362-007-0090-3.

[39] D. Robinson, Statistical Design: Chemometrics By R. E. Bruns, I. S. Scaramino, and B. De Barros Neto, Elsevier, Org. Process Res. Dev., 10- 5 (2006), 1082–1083. doi: 10.1021/op060138n.

[40] S. D. Brown, R. Tauler, and B. Walczak, Comprehensive Chemometrics: Chemical and Biochemical Data Analysis, Illustrated edition. Amsterdam: Elsevier, 2009. ISBN: 9780444527011

[41] S. D. Brown, Chemometrics: A textbook. D. L. Massart. B. G. M. Vandeginste, S. N. Deming, Y. Michotte, and L. Kaufman, Elsevier, Journal of Chemometrics, 2-4 (1988) 298–299. doi: 10.1002/cem.1180020409.

[42] G. Hanrahan and F. A. Gomez, Eds., Chemometric methods in capillary electrophoresis. Hoboken, N.J: Wiley, 2010. ISBN: 978-0-470-39329-1

[43] M. Feinberg, Experimental design: A chemometric approach, S. N. Deming and S. L. Morgan; from the series: “Data Handling in Science and Technology”, Elsevier, Journal of Chemometrics, 2-2, (1988) 169–169. doi: 10.1002/cem.1180020208.

[44] V. V. Lozenko and V. G. Shepelevich, Grain and subgrain structure of rapidly solidified Zn, Zn-Cd, Zn-Sn, and Zn-Sb foils, Inorg Mater, 43-1, (2007) 20–24. doi: 10.1134/S0020168507010062.

[45] T. Schmidt, F. Gärtner, H. Assadi, and H. Kreye, Development of a generalized parameter window for cold spray deposition, Acta Materialia, 54-3 (2006) 729–742. doi: 10.1016/j.actamat.2005.10.005.

[46] J. Pattison, S. Celotto, A. Khan, and W. O’Neill, Standoff distance and bow shock phenomena in the Cold Spray process, Surface and Coatings Technology, 202-8 (2008) 1443–1454. doi: 10.1016/j.surfcoat.2007.06.065.

List of figure captions

Figure 1. Spear uniform shell of experimental points in a Doehlert design (a) for 2 (points 1–7) and 3 (points 1–13) factors; (b) hexagon, cross section projection of the initial sphere [28].

Figure 2. SEM images a) of Zn powder and EDS analyses (inset), b) the size distribution measured with laser granulometer.

Figure 3. Determination of the limit temperature of deposition at constant pressure 20 MPa.

Figure 4. Three-points bending test Schematic illustration.

Figure 5. Surface analysis of roughness with a) optical microscope of zinc coating elaborated with 2.5 MPa pressure and 320 °C, b) Plot of dependence R_a and R_z on T for the difference (±0.01 mm).

Figure 6. SEM observations of coating cross section, elaborated with 260 °C and 2.5 MPa.

Figure 7. The SEM observations after etching in sulphuric acid with water at proportion 1:4.

Figure 8. X-ray diffractograms of Zn powder and as-sprayed Zn coatings.

Figure 9. 3D images of Zn coatings for different parameters: a) overview of coated system, b) 290 °C - 2 MPa.

Figure 10. a) σ–ε curves of Zn coating and b) observations of bended sample, 290 °C, 2 MPa.

Figure 11. Results of corrosion experiments for Zn coatings on carbon steel a) Open circuit potentials of Zn coatings in comparison with polished bulk Zn and steel substrate, b) Potentiodynamic polarization curves of Zn coatings, polished bulk Zn and steel substrate.

Figure 12. Zn coating on carbon steel 290 °C and 3 MPa, a) SEM photo of the coating after LSV, b) EDS analysis of Zn coating after LSV.

Figure 13. Hexagons based on Doehlert uniform shell design, correlation of spraying parameters T, P and a) interfacial porosity volume, b) thickness.

Figure 14. Hexagons based on Doehlert uniform shell design, correlation of spraying parameters T, P and Polarization resistance.

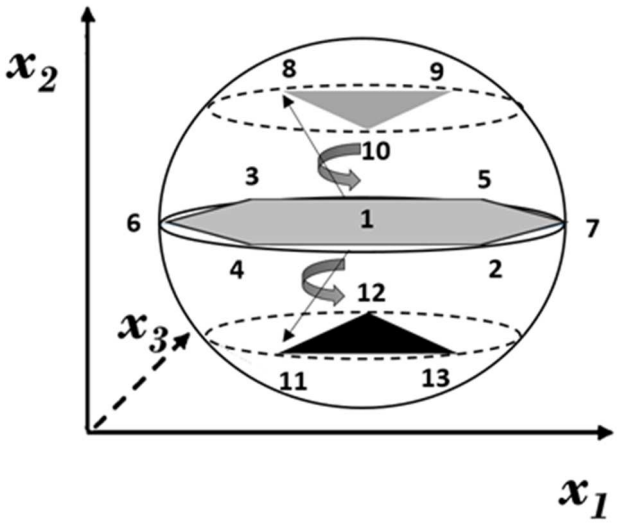

Figure 1. a

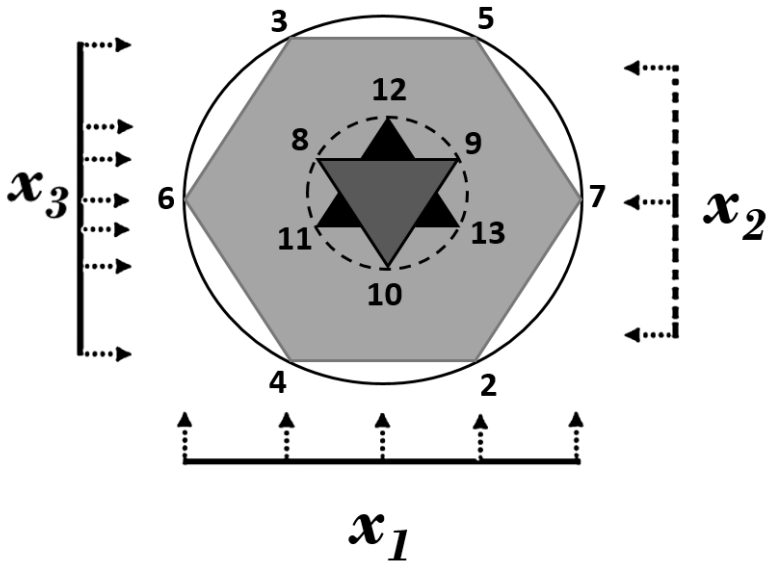

Figure 1. b

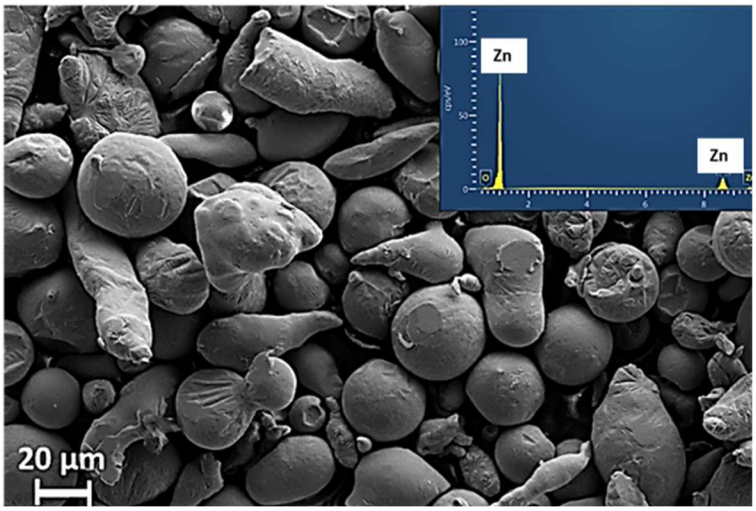

Figure 2. a

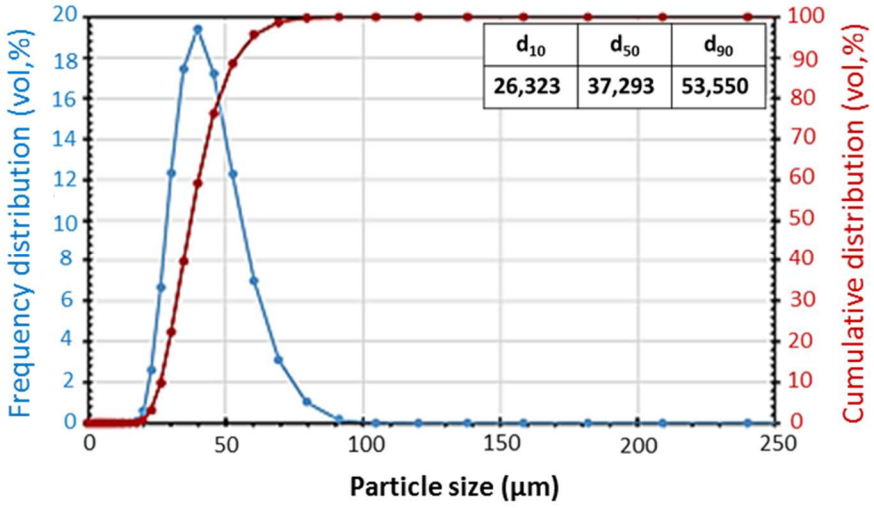
Frequency distribution (vol,%)
Cumulative distribution (vol,%)
Particle size (µm)
d10
d50
d90
26,323
37,293
53,550
0
2
4
6
8
10
12
14
16
18
20
0
10
20
30
40
50
60
70
80
90
100
0
50
100
150
200
250

Figure 2.b

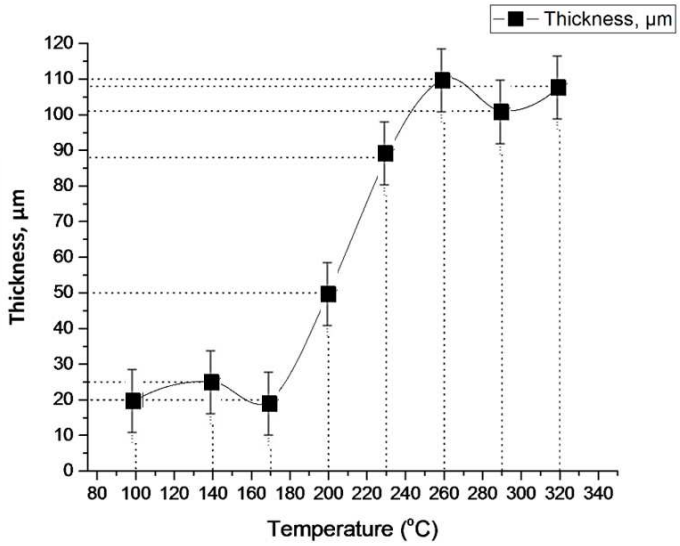
Thickness, µm
Thickness, µm
Temperature (°C)
0
10
20
30
40
50
60
70
80
90
100
110
120
80 100 120 140 160 180 200 220 240 260 280 300 320 340

Figure 3

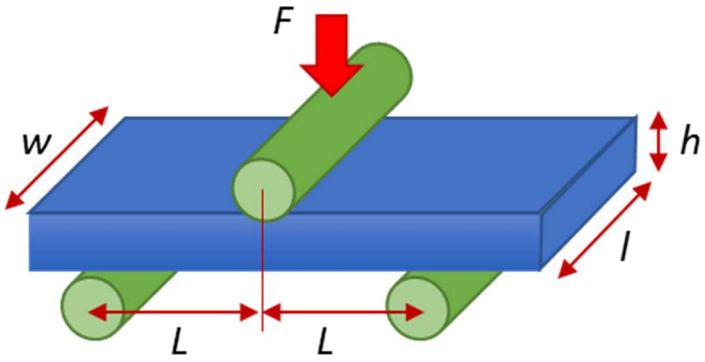

Figure 4.

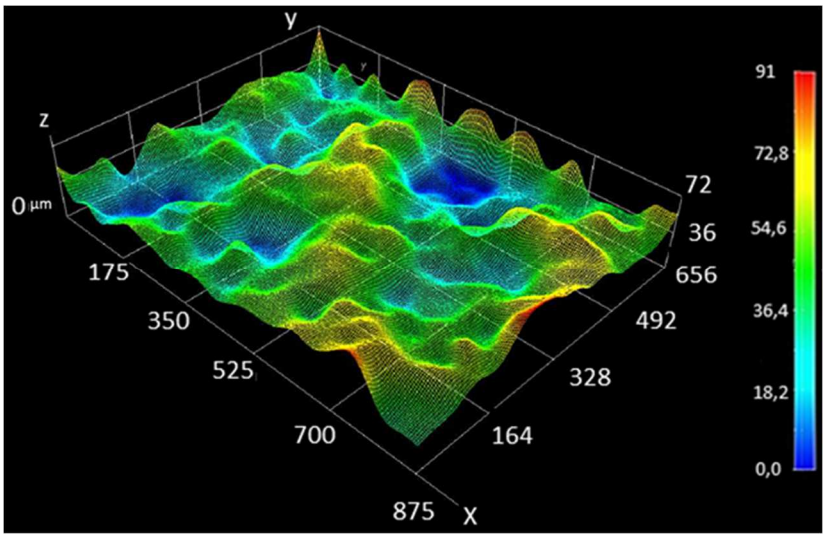
y
z
0 µm
175
350
525
700
875
X
72
36
656
492
328
164
91
72,8
54,6
36,4
18,2
0,0

Figure 5. a

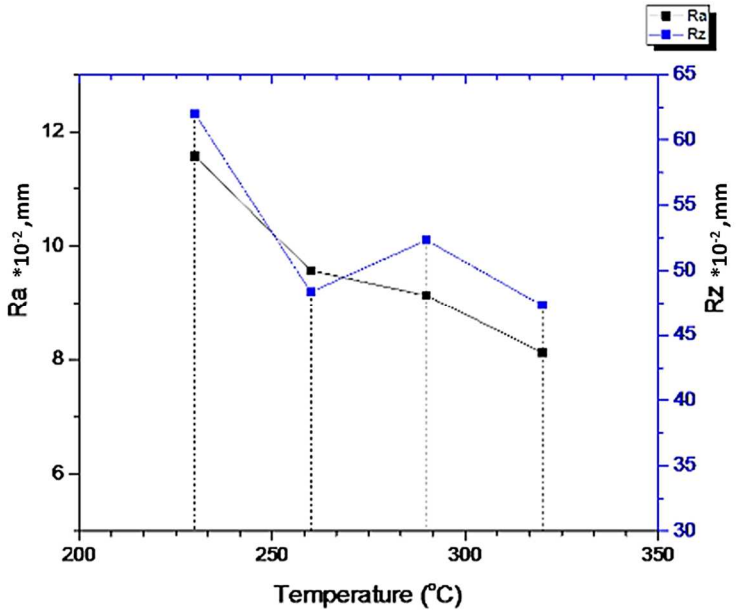
Ra
Rz
Ra *10-2,mm
Rz *10-2,mm
Temperature (°C)
12
10
8
6
65
60
55
50
45
40
35
30
200
250
300
350

Figure 5. b

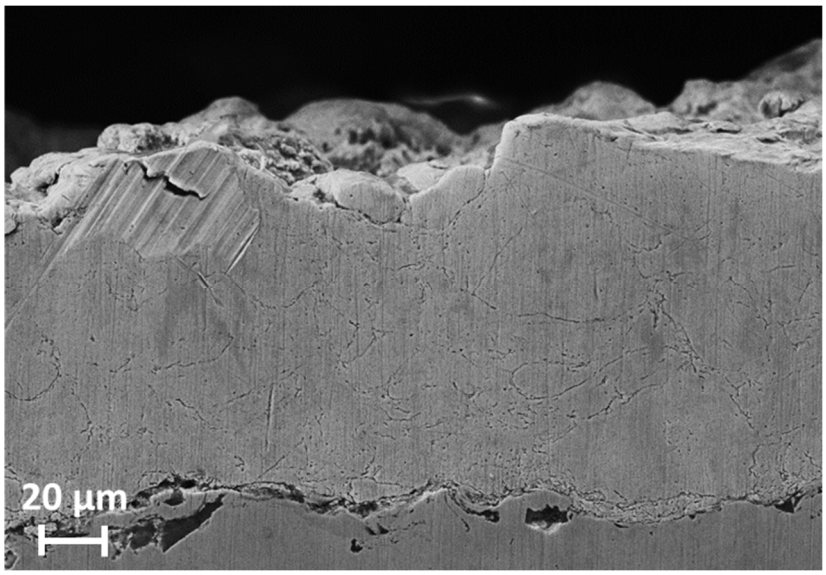

Figure 6

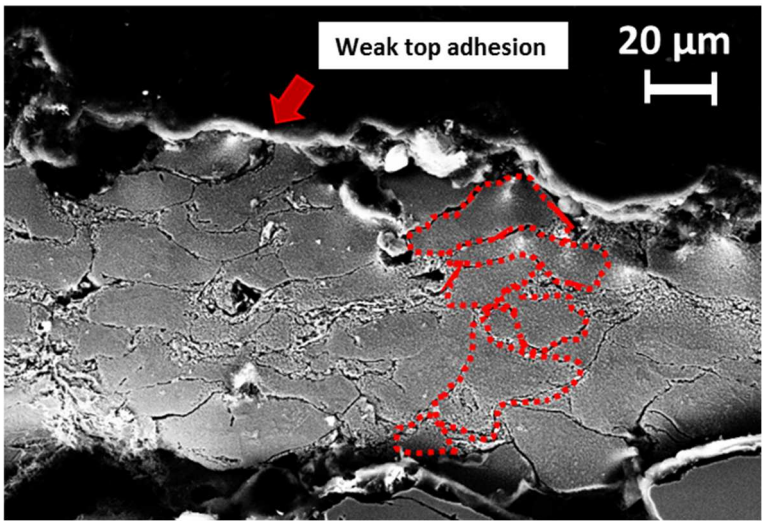

Figure 7

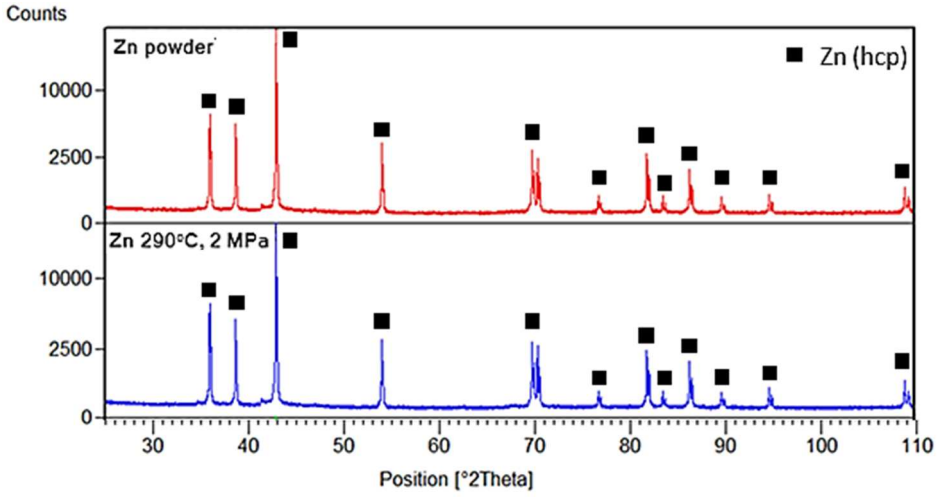
Counts
Zn powder
Zn (hcp)
10000
2500
0
Zn 290°C, 2 MPa
10000
2500
0
30
40
50
60
70
80
90
100
110
Position [°2Theta]

Figure 8

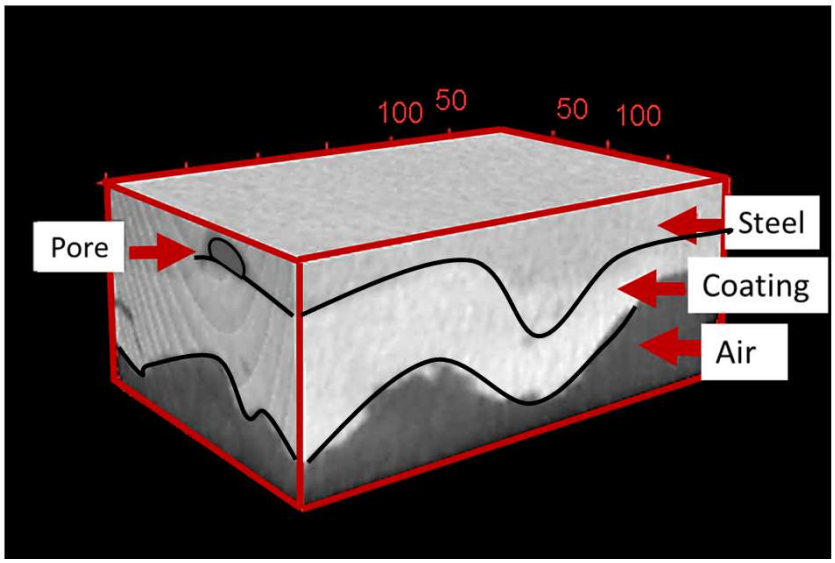

Figure 9.a

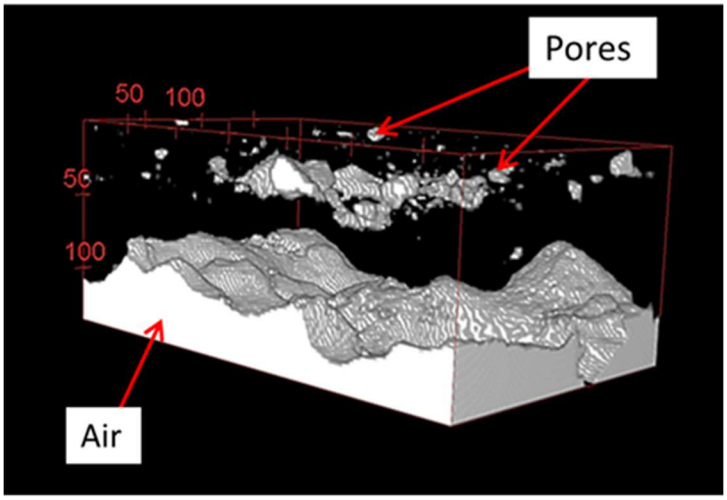

Figure 9.b

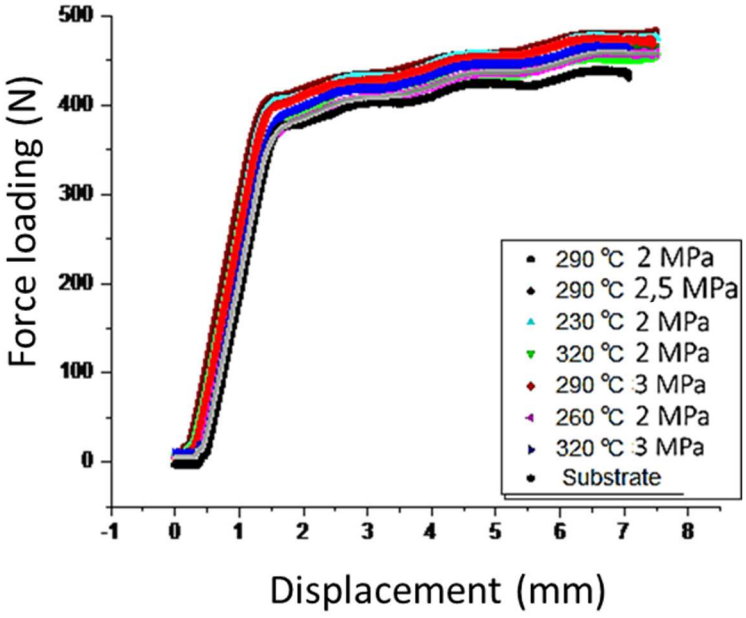
Force loading (N)
Displacement (mm)
290 °C 2 MPa
290 °C 2,5 MPa
230 °C 2 MPa
320 °C 2 MPa
290 °C 3 MPa
260 °C 2 MPa
320 °C 3 MPa
Substrate

Figure 10.a

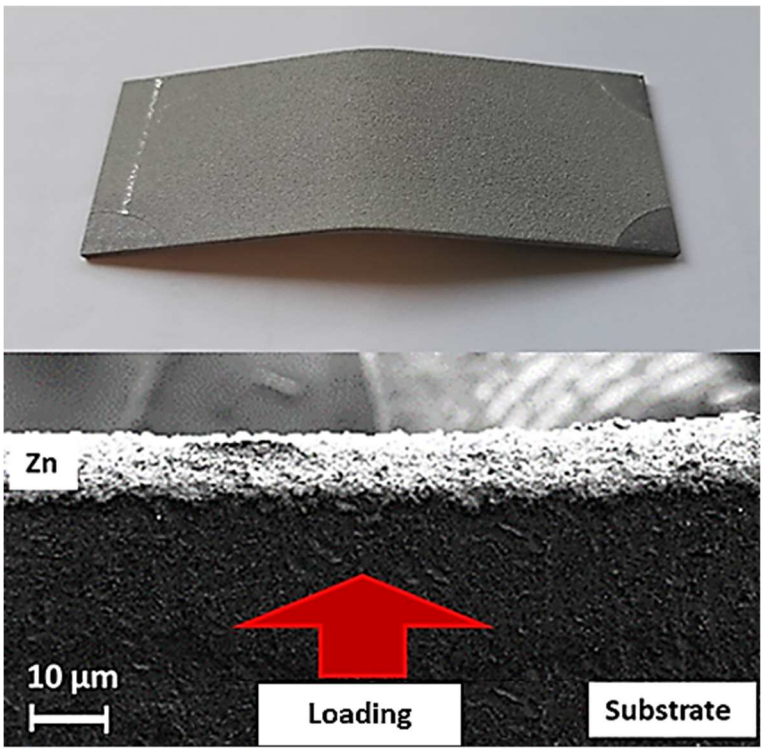

Figure 10.b

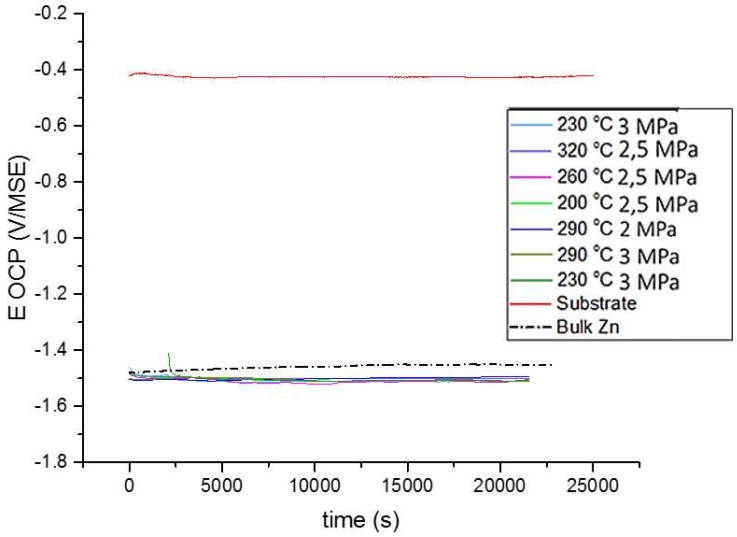
E OCP (V/MSE)
time (s)
-0.2
-0.4
-0.6
-0.8
-1.0
-1.2
-1.4
-1.6
-1.8
0
5000
10000
15000
20000
25000
230 °C 3 MPa
320 °C 2,5 MPa
260 °C 2,5 MPa
200 °C 2,5 MPa
290 °C 2 MPa
290 °C 3 MPa
230 °C 3 MPa
Substrate
Bulk Zn

Figure 11.a

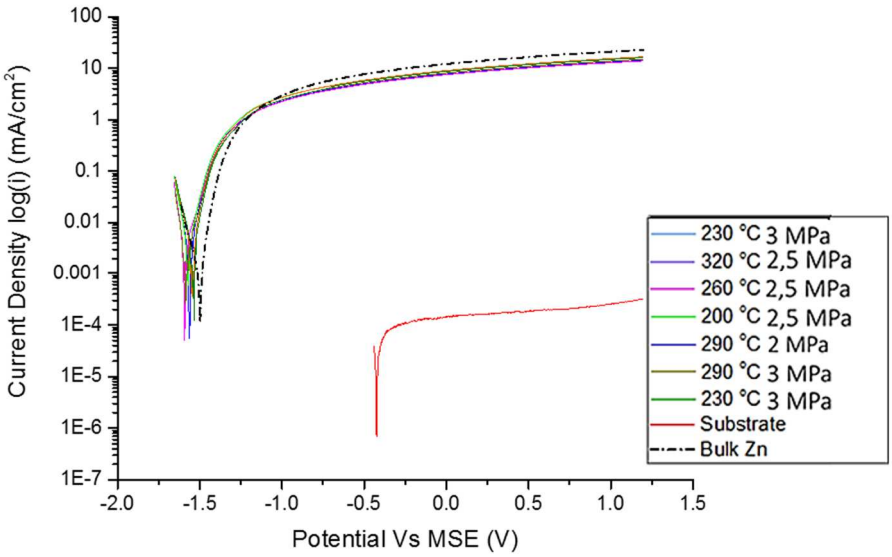
Current Density log(i) (mA/cm^2)
100
10
1
0.1
0.01
0.001
1E-4
1E-5
1E-6
1E-7
-2.0
-1.5
-1.0
-0.5
0.0
0.5
1.0
1.5
Potential Vs MSE (V)
230 °C 3 MPa
320 °C 2,5 MPa
260 °C 2,5 MPa
200 °C 2,5 MPa
290 °C 2 MPa
290 °C 3 MPa
230 °C 3 MPa
Substrate
Bulk Zn

Figure 11.b

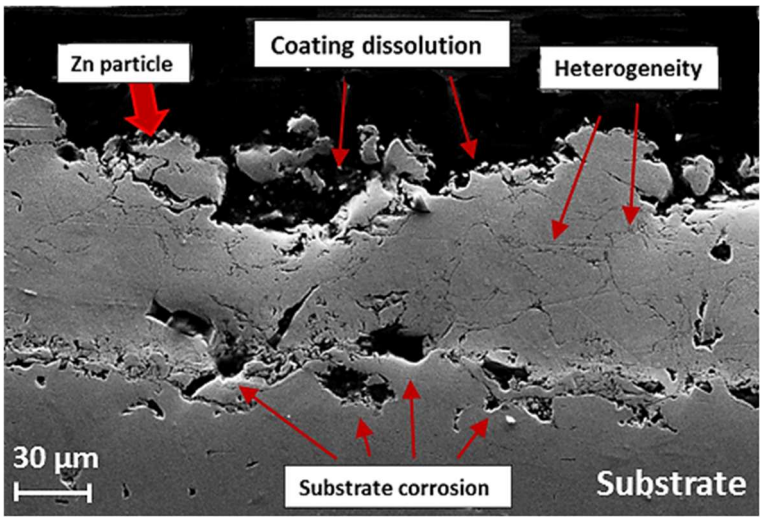
Zn particle
Coating dissolution
Heterogeneity
30 µm
Substrate corrosion
Substrate

Figure 12.a

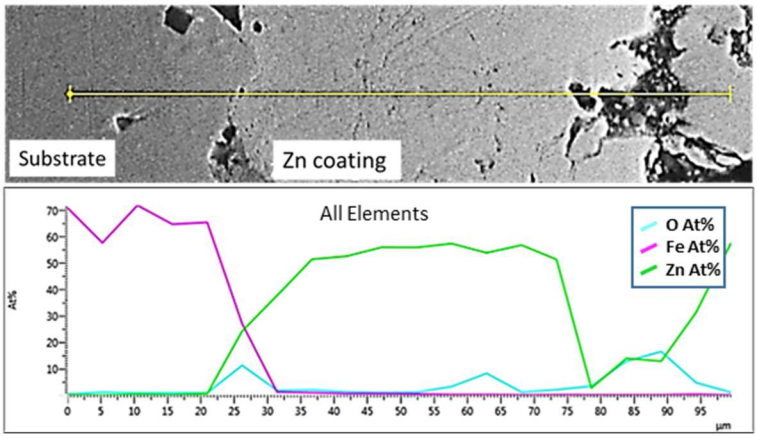
Substrate
Zn coating
All Elements
O At%
Fe At%
Zn At%
At%
70
60
50
40
30
20
10
0
5
10
15
20
25
30
35
40
45
50
55
60
65
70
75
80
85
90
95
µm

Figure 12.b

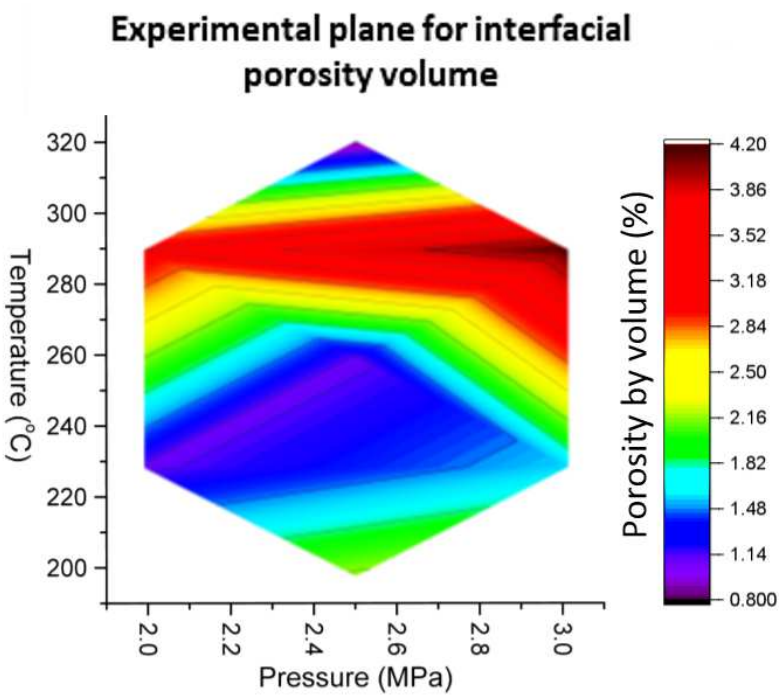
Experimental plane for interfacial porosity volume
Temperature (°C)
320
300
280
260
240
220
200
2.0
2.2
2.4
2.6
2.8
3.0
Pressure (MPa)
Porosity by volume (%)
4.20
3.86
3.52
3.18
2.84
2.50
2.16
1.82
1.48
1.14
0.800

Figure 13.a

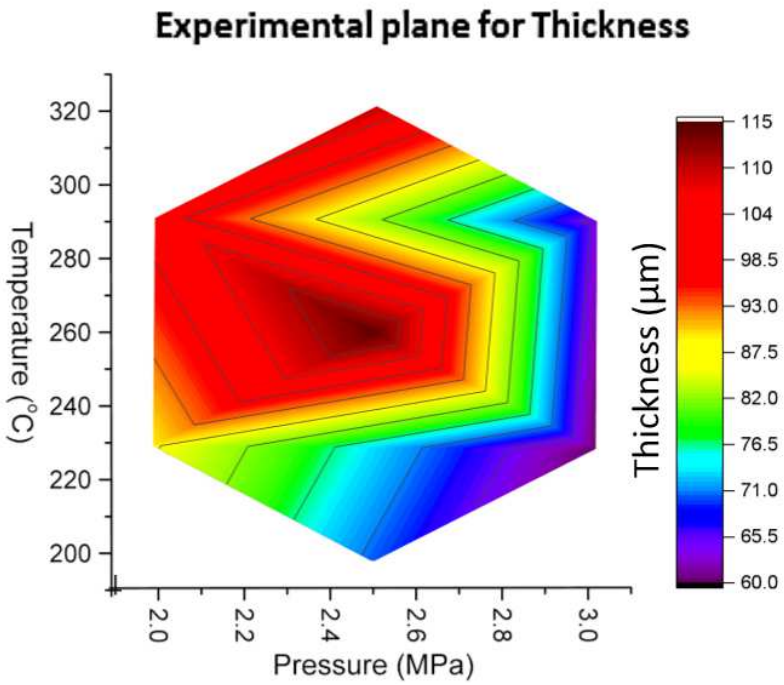
Experimental plane for Thickness
Temperature (°C)
320
300
280
260
240
220
200
2.0
2.2
2.4
2.6
2.8
3.0
Pressure (MPa)
Thickness (µm)
115
110
104
98.5
93.0
87.5
82.0
76.5
71.0
65.5
60.0

Figure 13.b

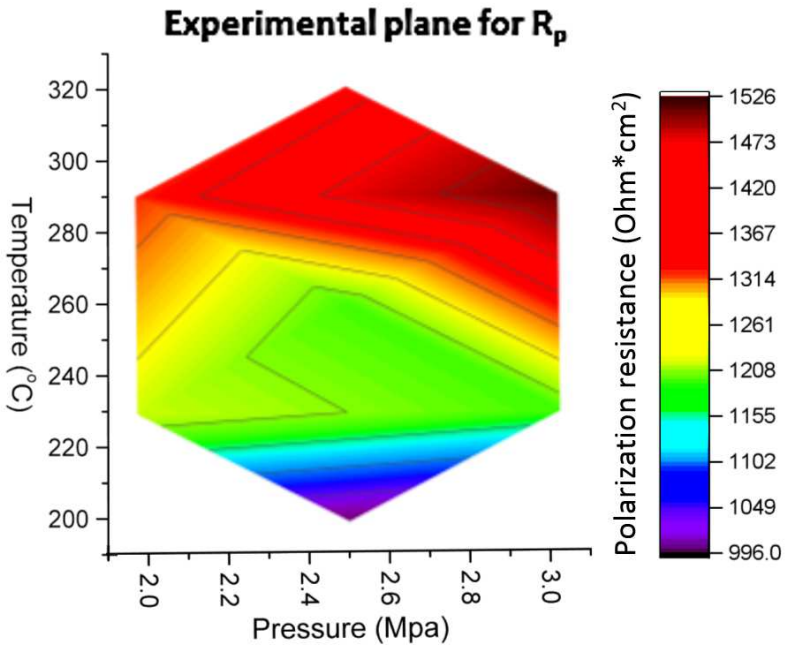
Experimental plane for R_p
Temperature (°C)
320
300
280
260
240
220
200
2.0
2.2
2.4
2.6
2.8
3.0
Pressure (Mpa)
Polarization resistance (Ohm*cm²)
1526
1473
1420
1367
1314
1261
1208
1155
1102
1049
996.0

Figure 14.

Table I. Rebuilt matrix with parameters taking into account to the temperature and gas boundaries conditions.

№	T, °C	P, MPa
1	260	2.5
2	320	2.5
3	290	3
4	200	2.5
5	230	2
6	290	2
7	230	3

Table II. Roughness maximum amplitudes in the area of 875x657 µm of each sample

Gas temperature, C^{o} (2 MPa)	100	140	170	200	230	260	290	320	Substrate
Roughness maximum amplitude, µm	62	86	75	84	89	119	103	91	51

Table III. Thickness of Zn coatings

Temperature, ^{o}C	200	230	230	260	290	290	320
Pressure, MPa	2.5	2	3	2.5	2	3	2.5
Thickness,±10 μm	70	88	60	115	101	64	108

Table IV. Interface porosity values of Zn coatings in volume

Temperature, °C	200	230	230	260	290	290	320
Pressure, MPa	2.5	2	3	2.5	2	3	2.5
Porosity V, %	2.2	1.1	0.8	1.1	3.2	4.2	0.8

Table V. Corrosion values of samples according to Doehlert design

Sample name	**E_{corr} (mV)**	**R_p (Ohm.cm^{-2})**	**I_{corr} (µA.cm^{-2})**
200 °C 2.5 MPa	-1581.9	996.5	21.2
290 °C 2 MPa	-1568.8	1339	19
320 °C 2.5 MPa	-1574.3	1346.8	11.9
230 °C 3 MPa	-1601.2	1180.8	10.8
230 °C 2 MPa	-1545.7	1234.8	11.6
260 °C 2.5 MPa	-1595.4	1183	13.2
290 °C 3 MPa	-1590,7	1524.6	10
Zn	-1501.3	3511.5	7.1
Substrate	-1049.6	983.4	0.0027